Supplemental Material for the manuscript "Persistent half-metallic ferromagnetism in a (111)-oriented manganite superlattice"

Fabrizio Cossu,[1,2] Heung-Sik Kim,[1,*] Biplab Sanyal,[3] and Igor Di Marco[2,3,4,†]

[1] *Department of Physics and Institute of Quantum Convergence and Technology, Kangwon National University – Chuncheon, 24341, Korea*

[2] *Asia Pacific Center for Theoretical Physics – Pohang, 37673, Korea*

[3] *Department of Physics and Astronomy, Uppsala University, Box 516, SE-75120, Uppsala, Sweden*

[4] *Department of Physics, POSTECH, Pohang, 37673, Korea*

(Dated: March 15, 2022)

This Supplemental Material contains additional information on the computational settings, the structural relaxation, the charge-density distributions and the inter-atomic exchange couplings. Finally, results for the bulk $LaMnO_3$ and $SrMnO_3$ are also reported, for sake of comparison.

PACS numbers: 75.70.Cn

* H.-S. Kim: heungsikim@kangwon.ac.kr

† I. Di Marco: igor.dimarco@apctp.org

I. SUPPLEMENTARY METHODS

Electronic structure calculations were performed with VASP and RSPt, as explained in the main text. For VASP, the basis set used included $4s^2 4p^6 5s^2 6d^1$, $4s^2 4p^6 5s^2$, $3s^2 3p^6 4s^2 3d^5$ and $2s^2 2p^4$ as valence states for La, Sr, Mn and O, respectively. For structural relaxations, the Brillouin zone was sampled using a $7 \times 7 \times 1$ k-mesh and a Gaussian smearing of 0.01 eV, while an energy tolerance of 1×10^{-5} eV and a force tolerance of 5×10^{-3} eV Å^{-1} are used. For the calculation of the DOS, the **k**-mesh density was increased to $15 \times 15 \times 2$ and the integrals in the Brillouin zone were performed through the tetrahedron method with Blöchl corrections. In this case, the energy tolerance was decreased to 1×10^{-7} eV. The kinetic energy cut-off of the plane waves was set to 500 eV for all calculations.

For RSPt, the space was physically divided in muffin-tin spheres and an interstitial region. In a full-potential method, this division is only formal and does not affect the quality of the calculations [1]. The radii of the muffin-tin spheres were chosen as 1.8, 2.6, 2.5 and 1.75 a.u. for respectively Mn, Sr, La and O, in order to ensure that the minima of the effective potential are located in the interstitial region. The basis set was constructed from $3s$, $3p$, $4s$, $4p$ and $3d$ states for Mn, $4s$, $4p$, $5s$ and $5p$ states for Sr, $5s$, $5p$, $6s$, $6p$ and $5d$ for La, $2s$ and $2p$ for O. The description of the wavefunctions in the interstitial region required the usage of two kinetic energy tails κ^2, equal to -4.1 eV and -20.4 eV. Calculations with sDFT+$U|J$ were performed using the implementation of Ref. 2, which corresponds exactly to the approach used in VASP, in absence of spin-orbit coupling. The inter-atomic exchange parameters J_{ij} were computed via finite temperature Green's function formalism [3, 4]. The local projectors were constructed from the muffin-tin heads, as for the "MT" basis in our previous works [2, 3]. Integrals in the Brillouin zone were performed via thermal smearing, for an effective temperature of about 160 K. The Brillouin zone was sampled with a dense Monkhorst-Pack grid of $11 \times 11 \times 1$ **k**-points. Convergence with respect to temperature and k-points was accurately checked.

II. SUPPLEMENTARY DISCUSSION

The supercell to optimize was composed of three (111)-oriented $R\bar{3}c$ units, where the atoms were allowed to arrange in a $a^-a^-a^-$ tilting pattern [5]. For clarity, the tilting pattern

for bulk $LaMnO_3$ and $SrMnO_3$ is shown in Supplementary Figure 1. Note that, with the stacking along (111), a unit cell includes 3 layers (15 atoms); the rotations, $a^-a^-a^-$ enhance the degrees of freedom and thus the unit is 6 layers (30 atoms); in order to take into account different magnetic orders and also other tilting systems, further degrees of freedom have to be introduced, allowing an in-plane doubling of the cell. We would also like to mention that, as the stacking is different between (111) and (001), there is no sharp correspondence between thicknesses in the two crystallographic orientations. Moving toward the (001) direction, we can cross 3 [111] planes for each (001) layer.

The tilting angles were initially optimized within each $R\bar{3}c$ unit, composed of 30 atoms. Then, each unit was used to build the superlattice, which was again fully relaxed. As reported in the main text, the ground-state is a half-metallic ferromagnet, which significantly more favourable than the competing anti-ferromagnetic phases. Alongside the tilted structure R^-, we also investigated how the system behaves if no tilts are allowed. This structure R^0 is significantly less favorable in energy, which shows the importance of the structural deformation. The energy difference between the two ferromagnetic states with and without tilts amounts to about 95.7 meV. A visualization of these two ferromagnetic structures is provided in Supplementary Figure 2.

Let us now focus on the ground state. The R^- structure undergoes minor relaxations compared to the initial input, i.e. the tilted components mentioned above; in particular, the octahedra tilts in input – 8.5° for $LaMnO_3$ and 4.8° for $SrMnO_3$ – vary smoothly across the superlattice, taking values between 8.3° and 9.9° in the $LaMnO_3$ region and between 4.7° and 6.7°in the $SrMnO_3$ region; angles and volumes in the $LaMnO_3$ ($SrMnO_3$) region are smaller (larger) at the interface, see the Q_1^R curve in Fig. 2 in the main text. The Mn nominal charge is +3 in the $LaMnO_3$ region and +4 in the $SrMnO_3$ region, inducing a charge transfer across the interface. This charge transfer is slightly reduced by the tilts (0.01 electrons difference is found between R^- and R^0 in both regions). In the R^- structure, the $SrMnO_3$ region gains electrons at the expense of the $SrMnO_3$ region. The opposite happens in the R^0 structure. Tilts also affect the magnitude of charge and spin disproportionation: without tilts, the amplitude of the oscillations of Mn charge and magnetic moments (see main text) is decreased by a factor 4.

To check the stability of our $a^-a^-a^-$ tilting, in the present study we tried another structure with a $a^-a^-c^+$ order, of which in-plane unit cell size being twice larger than that of the

$a^-a^-a^-$ unit cell. As shown in Fig. 1(b) in the main text, the $a^-a^-a^-$ structure becomes stabler upon the introduction of in-plane compressive strain of 1.5%. Note that the main observations of this study — the half-metallic character with Mn charge and spin oscillation — remains valid in the $a^-a^-c^+$ system as well, which we would like to investigate in more detail in a future study.

Finally, a comment on our choice of in-plane lattice parameters. We have performed the calculation of electronic properties using two different in-plane lattice constants (with the out-of-plane constant being optimized accordingly); 3.860 Å and 3.892 Å, where the former is the one optimized from full unit cell relaxation (*i.e.* minimizing the stress tensor), while the latter is the average of bulk lattice parameters of $LaMnO_3$ and $SrMnO_3$. The latter corresponds to less than 1% of tensile strain with respect to the former, and shows only marginal differences in structural, electronic, and magnetic properties including the separation of t_{2g} and e_g orbitals, the nature of the band-gap in the minority-spin channel, and the smooth variation of the band on-sets across the superlattice, compared to the former. For technical reasons, some of the results (Figs. 4 and 6 in the main text, and Supplementary Figures 3, 4, 6, 8, 9 and 10) were presented using the in-plane parameter of 3.892 Å.

To verify the accuracy of our methods and to better contextualize our results, it is useful to show the results obtained for the bulk systems. These calculations were performed in sDFT+U, as discussed in the main text. The Coulomb interaction parameters were chosen as for the superlattice, i.e. $U = 3.8$ eV and $J = 1.0$ eV. The relative energies of the competing magnetic phases as well as the local magnetic moments on the Mn atoms are reported in Table I. For clarity, positive energies correspond to a FM ground state, while negative values correspond to an AFM ground state (A-type or G-type, see the caption). For $SrMnO_3$, the magnetic moment of the AFM state is in line with the experimental value of 2.6 μ_B reported in Ref. 6. The energy difference between the AFM and FM states is also in very good agreement with the value of about 92 meV recently obtained with the GGA+U approach in Quantum Espresso, by Ricca *et al.* [7]. For $LaMnO_3$, the magnetic moment of the AFM state is also in line with the value of 3.87 μ_B obtained from neutron diffraction experiments [8], considering the experimental error bars. A better agreement is found with theoretical works, as e.g. with the value of 3.63 μ_B obtained via VASP calculations based on the SCAN exchange-correlation functional [9]. A GGA+U study [10] based on the VASP code also provided a good agreement with our work, namely a magnetic moment of 3.65 μ_B

and an energy difference between FM and AFM states of about 13 meV per formula unit. This energy is slightly larger than ours due to the fact that the authors used a smaller value of U. This small discrepancy is perfectly consistent with the large set of data reported in a recent work [11]. Table I also illustrates values for the pseudocubic systems, which offer a better comparison with the local environment inside the superlattice. Two tilting systems are reported, as well as two possible lattice constants, namely the full pseudocubic relaxation and the lattice constant corresponding to the superlattice. From Table I we can observe the magnetism of $LaMnO_3$ is strongly affected by the transition to a pseudocubic phase, accompanied by a small strain, as all systems turn to be FM. Additionally, we observe two trends. First, the magnetic moments do not depend much on the details of the pseudocubic phases. Second, the stability of the ferromagnetic phase increases when the tilting system goes from $a^-a^-c^+$ to $a^-a^-a^-$ as well as when the lattice constant decreases from the pseudocubic relaxed value to the superlattice value. Overall, going from the $LaMnO_3$ to the pseudocubic system with the lattice constant of the superlattice leads to a substantial increase of the stability of the FM phase, which we believe has a crucial role in determining the properties of our superlattice.

The role of the charge transfer can also be analyzed by doping the system, which in DFT can be achieved by treating the excess charge as a uniform background. VASP calculations were performed by doping the superlattice with ± 2.0 electrons, which corresponds to ± 0.11 electrons per formula unit. This is not only useful to analyze the role of the charge transfer, but also to understand how the system will behave with respect to intrinsic doping, due to impurities occurring during the growth process. The resulting magnetic moments at the Mn atoms are reported in Supplementary Figure 3. In the bottom panel, we can see that, starting from charge neutrality, decreasing the total charge leads to a slight increase in oscillations in the $LaMnO_3$ region (for -0.5 electrons), which is followed by a gradual decrease. The oscillations disappear for a doping of -2.0 electrons. A reserved trend is observed in the $SrMnO_3$ region, where the oscillations increase with the hole doping (for the values explored). Interesting, for all the curves in the bottom panel, the magnetism remains pinned in the two bulk regions, and the largest Mn magnetic moments are found in the layers that are farthest from the interface. In the top panel, the data for electron doping are reported. When the total charge is increased, the oscillations in the $LaMnO_3$ region first increase (for +0.5 electrons) and then decrease, which is also accompanied by a phase change

of the high-low spin values. A total quenching of the oscillations is reached for a doping of +2.0 electrons, when the curve becomes flat. This trend persists also for larger doping (data not shown). A different behavior is observed in the $SrMnO_3$ region. An increasing charge leads to a parabolic curve, whose minimum value is in the middle of the bulk-like region. Overall, we see that the oscillating behavior of the magnetization is strongly connected to the occupation of the Mn-3d states and variations as small as ± 0.11 electrons per formula unit lead to a smoother trend. It is interesting to see how this trend reflects on the different types of van Vleck distortions, shown in Supplementary Figure 4. Doping the superlattice with 1 additional electron (top panel) makes the Jahn-Teller distortions Q_2^R and Q_3^R larger than in the undoped case. Conversely the breathing modes of Q_1^R decrease slightly, which is accompanied by a phase shift (offset). If the doping is increased to 3 electrons (bottom panel), the breathing modes in Q_1^R disappear and are replaced by a smooth variation of the van Vleck distortion across the superlattice. Moreover, the Jahn-Teller modes Q_2^R become substantial, although their maximum value in the middle of the $LaMnO_3$ region is still the half of the corresponding bulk value [12]. Conversely, Q_3^R seems to be twice as large as its corresponding bulk value [12].

As a final note, we point out that, in the R^0 structure, where the tilts are removed, the oscillatory pattern is reduced, due to a decreased kinetic energy (data not shown).

Supplementary Figure 5 illustrates the charge density difference at the interface in the superlattice, with (panel a) and without (panel b) octahedral tilts. The A-cations (Sr, La) determine the occupancy of the Mn on different regions, driving an electronic reconstruction (charge transfer) [13] across the interface. As discussed in the main text, the strain induced by the superlattice formation and the stacking due to the (111) orientation induce a half-metallic ferromagnetic character. As a result, the charge transferred across the various interfaces is larger for the (111)-oriented superlattices than for their (001) counterpart [14–16]. As shown in Supplementary Figure 5, octahedral tilts reduce this effect. It is also interesting to look at the Mn-3d charge projected over real spherical harmonics across the superlattice, reported in Supplementary Figure 6. We can observe that the t_{2g} states are almost constant over the whole structure. Conversely, the charge oscillations are entirely defined in terms of the e_g states. It is also interesting to note that the e_g states become different inside the $LaMnO_3$ region.

The layer-projected partial density of states (DOS) for Mn-3d and O-2p states is shown in

Supplementary Figure 7. Here we can see how the half-metallic character persists well inside the $LaMnO_3$ and $SrMnO_3$ regions. This is very different from what is observed in (001)-oriented superlattices, where the half-metallic character is strictly localized the interface for a $LaMnO_3$ side thicker than 2 formula units, as discussed in the main text. Another interesting feature noticeable in Supplementary Figure 7 is the behavior of the O bands, which are pushed up towards the Fermi level in the $SrMnO_3$ region by more than 1eV. Furthermore, their spectral value, which in the $LaMnO_3$ and interfacial regions is below that of the Mn, exceeds this inside the $SrMnO_3$ region.

Still at the interface, the charge density maps show – see Supplementary Figure 8 – that an orbital order occurs for $\mathrm{E} - \mathrm{E}_F = (-0.36\,;\,0.00)\,\mathrm{eV}$. At the Fermi level, electrons populate the $d_{y^2-z^2}$ orbitals in the inner $SrMnO_3$ region and the $d_{x^2-y^2}$ orbitals in the $LaMnO_3$ region.

In Supplementary Figure 8, the magnetization density distribution is reported, for three different energy ranges. We note that the charge density distribution shows very similar features and therefore is not shown. For the energy range $(-5.95\,;\,-5.35)\,\mathrm{eV}$, illustrated in the top panel, the d_{xy} orbital (as projected onto the local reference frame of the octahedra) dominates in the $LaMnO_3$ region, while a mix of all t_{2g} orbitals (a_{1g}) dominates in the $SrMnO_3$ region. In the same energy range, in the $LaMnO_3$ region, electrons populate the O p orbitals in the direction of the Mn-O bond; however, for each Mn site, p_z, p_y and p_x appear fully occupied, partially occupied and empty, respectively. Note also the antiferromagnetic coupling between the Mn d and O p, which is observed in R^-, but not in R^0 for this particular energy range. Because of the quasi-cubic environment, t_{2g} orbitals are degenerate; however, the direct-space maps show that t_{2g} and e_g orbitals within the ranges of charge and magnetic moments modulations have a preferred axis and do not fall in the a_g, e_g^1 and e_g^2 orbital order.

We can observe orbital order in the $SrMnO_3$ region around the Fermi level, whereas at lower energies a mixture of the t_{2g} orbitals is seen, indicating degeneracy in the $SrMnO_3$ region.

Finally, we also observe that direct-space maps, as well as the analysis of the Bader charges (not shown), do not have any charge oscillation associated to the O atoms, at variance with the case of (001)-oriented superlattices recently investigated by resonant X-ray scattering (RXS) [17].

The magnetic properties have been calculated with RSPt. In Supplementary Figure 10, the magnetic moments of the Mn-3d states are reported, alongside the corresponding values

obtained with VASP. These data show that the two codes are in good agreement with each other. The small differences are due to technical details, as e.g. the different basis set used for the local projects, as well as the different sizes of the atomic regions considered. From Supplementary Figure 10, one can also notice that the magnetic moments are entirely defined by their $3d$ components. The contributions from the sp states is at most 0.02 μ_{B}, which is about 0.5% of the total values.

The corresponding inter-atomic exchange couplings J_{ij} between Mn-$3d$ states for atoms belonging to different layers are shown in Supplementary Figure 9. As one can see the most significant contributions correspond to the first and fourth nearest neighbors. For each shell, there are 6 neighbors whose couplings have a two-fold degeneracy, depending on what direction they point to, with respect to the superlattice orientation. Each group of 3 values exhibit differences that are smaller than 1% of their average. The 2 average values for each shell are illustrated in Fig. 3 of the main text. The inter-atomic exchange couplings of the other shells of neighbors are much smaller. Among them, the coupling with the eighth nearest neighbors is the largest, but in the scale of the figure this contribution is visible only for the layers inside the $SrMnO_3$ region, i.e. 13 to 17, where it appears to be about one fourth of the coupling with the forth nearest neighbors.

To ensure that our computational approach (in particular our choice of the Coulomb interaction parameters in the sDFT+U|J and cDFT+U|J schemes) does not introduce an artificial bias in our results, we performed additional calculations employing Strongly Constrained and Appropriately Normed (SCAN) semi-local exchange-correlation functional [18]. These results are in consistency with those obtained from our sDFT+U calculations, especially in terms of the spin and charge oscillations in the half-metallic $a^-a^-a^-$ tilting system as obtained from our SCAN calculation and shown in Supplementary Figure 11. Two noticeable things are found.

i Mn charges in the SCAN result are suppressed by $\sim$ 0.08 per site across the whole superlattice compared to the sDFT+U result; this is the result of the more enhanced change transfer from Mn to O due to the enhanced orbital energy splitting between Mn d and O p in SCAN than in sDFT+U.

ii The charge and spin oscillations are suppressed in the SCAN case compared to those of sDFT+U result; this can also be attributed to the electron transfer from Mn to O

occurring in the SCAN case, effectively hole-doping the whole Mn sites by $\Delta N \simeq -1.4$ e / unit cell.

As shown in the bottom panel of Supplementary Figure 3, introducing a hole doping of $\Delta N > -1$ e / unit cell tends to suppress the magnitude of spin oscillation in the $LaMnO_3$ layers. The origin of the enhanced charge transfer and its results in the SCAN result needs further analyses, which we would like to pursue in a future study.

III. SUPPLEMENTARY FIGURES AND TABLES

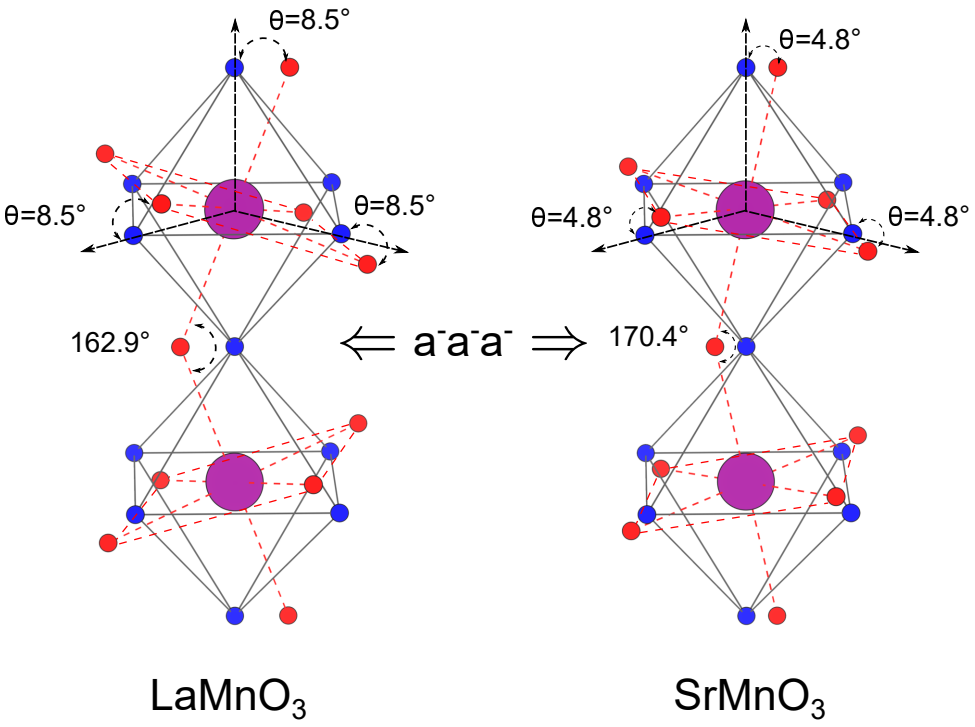

Supplementary Figure 1. (Colour online) MnO_6 octahedral tilt in bulk $R\bar{3}c$ $LaMnO_3$ (left) and bulk $SrMnO_3$ (right), relative to the ideal, undistorted structure. The angles are exaggerated for illustrative purposes.

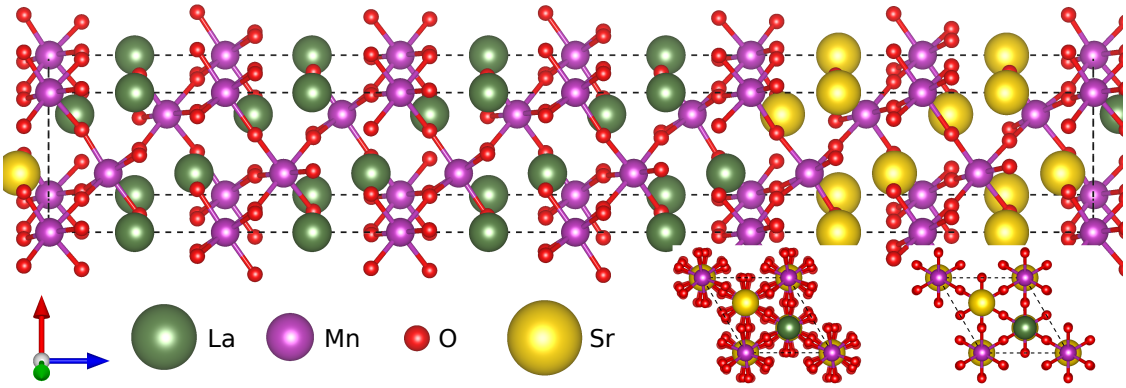

Supplementary Figure 2. (Colour online) Side view of the ferromagnetic ground-state structure of the superlattice R^-. At the bottom the top view of this structure is shown, alongside the top view for the R^0 structure, without tilts.

Supplementary Table I. Energy difference $\Delta E = E_{\rm AFM} - E_{\rm FM}$ per formula unit for different bulk-like structures. The AFM state is G-type for $SrMnO_3$ and A-type for $LaMnO_3$. The 2 bulk structures are obtained for the experimental lattice parameters [7, 10], namely (3.99,3.99,3.86) $\mathring{A}$ for the orthorhombic phase of $LaMnO_3$ and 3.80 $\mathring{A}$ for the cubic phase of $SrMnO_3$. In addition, for $LaMnO_3$, 4 pseudocubic structures are also shown, corresponding to 2 different tilting systems, with the lattice constant fully relaxed ($a = 3.885$ Å) or constraint to the value used for the superlattice ($a_0 = 3.860$ Å).

	$SrMnO_3$	$LaMnO_3$				
	bulk	bulk	$a^-a^-c^+$	$a^-a^-a^-$	$a^-a^-c^+$ at a_0	$a^-a^-a^-$ at a_0
ΔE (meV)	-99.2	-8.3	18.5	21.9	24.8	27.1
$\mu_{\rm FM}$ (μ_B)	2.60	3.61	3.67	3.67	3.65	3.67
$\mu_{\rm AFM}$ (μ_B)	2.58	3.56	3.55	3.56	3.54	3.55

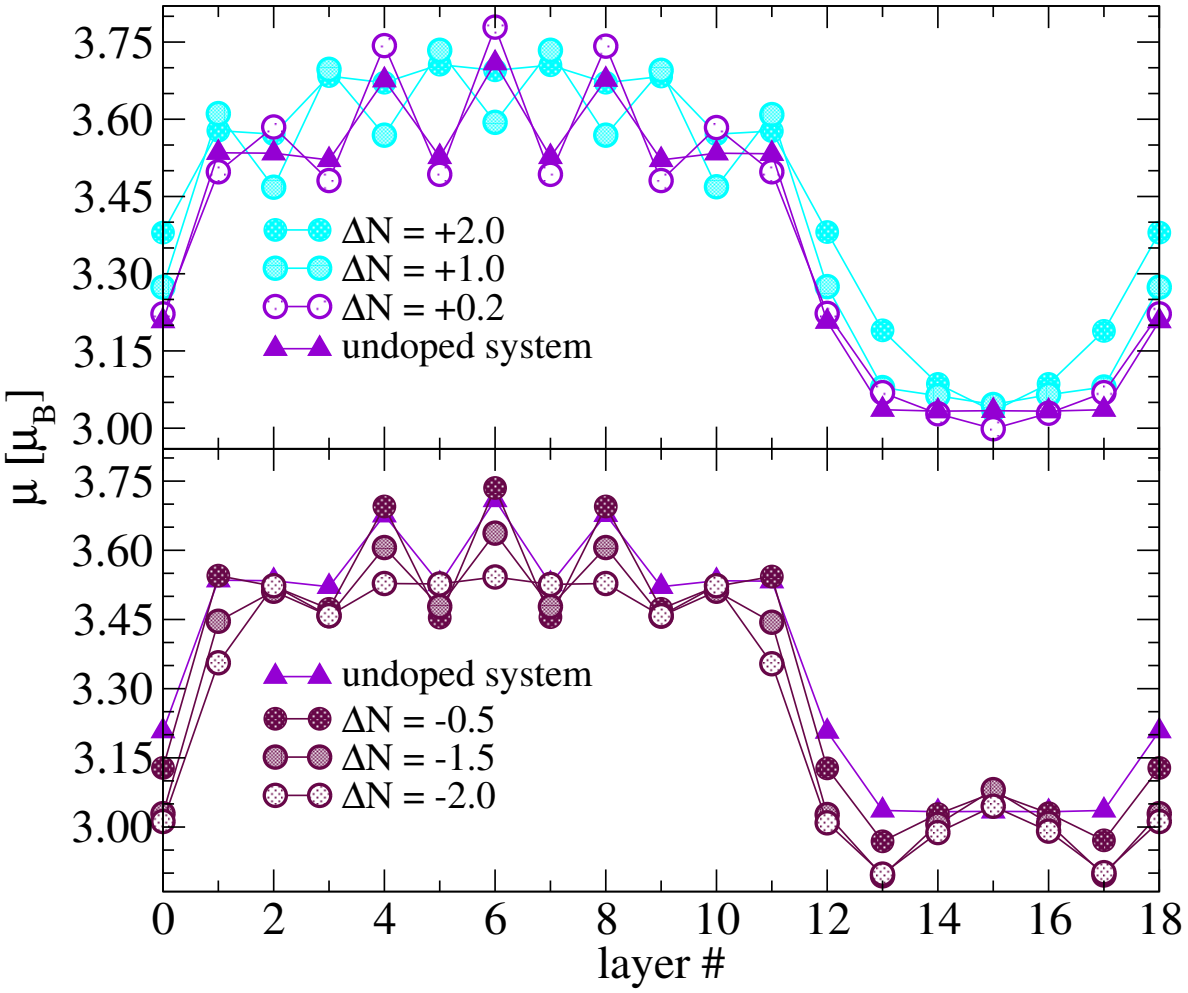

Supplementary Figure 3. Total magnetic moments at the Mn atoms in different layers, for electron doping (top panel) and hole doping (bottom panel).

IV. SUPPLEMENTARY REFERENCES

[1] http://fplmto-rspt.org.

[2] Grånäs, O. *et al.* Charge self-consistent dynamical mean-field theory based on the full-potential linear muffin-tin orbital method: Methodology and applications. *Comput. Mater. Sci.* **55**, 295–302 (2012).

[3] Kvashnin, Y. O. *et al.* Exchange parameters of strongly correlated materials: Extraction from spin-polarized density functional theory plus dynamical mean-field theory. *Phys. Rev. B* **91**,

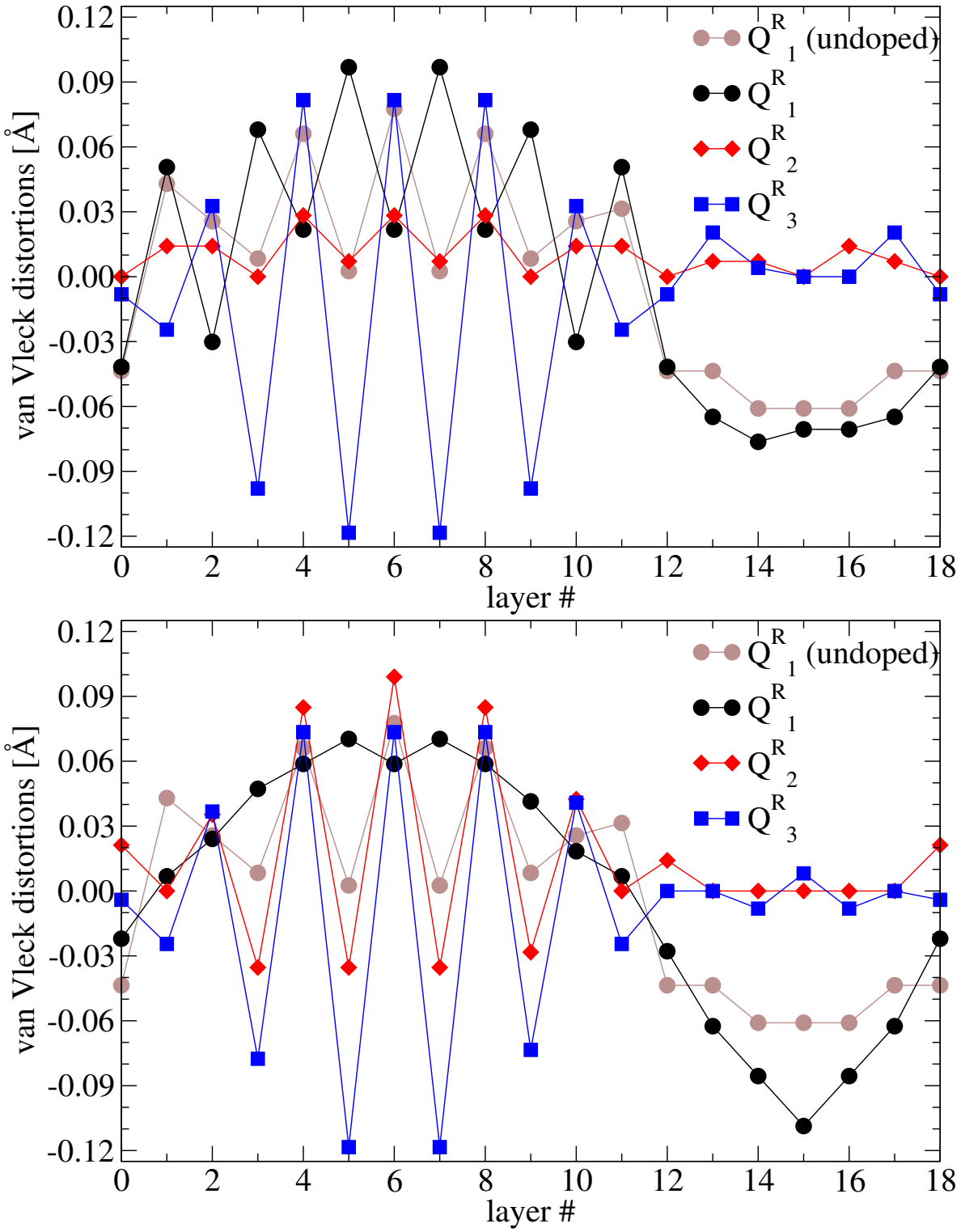

Supplementary Figure 4. Van Vleck distortions for an electron doping of 1 electron (top panel) and 3 electrons (bottom panel).

125133 (2015).

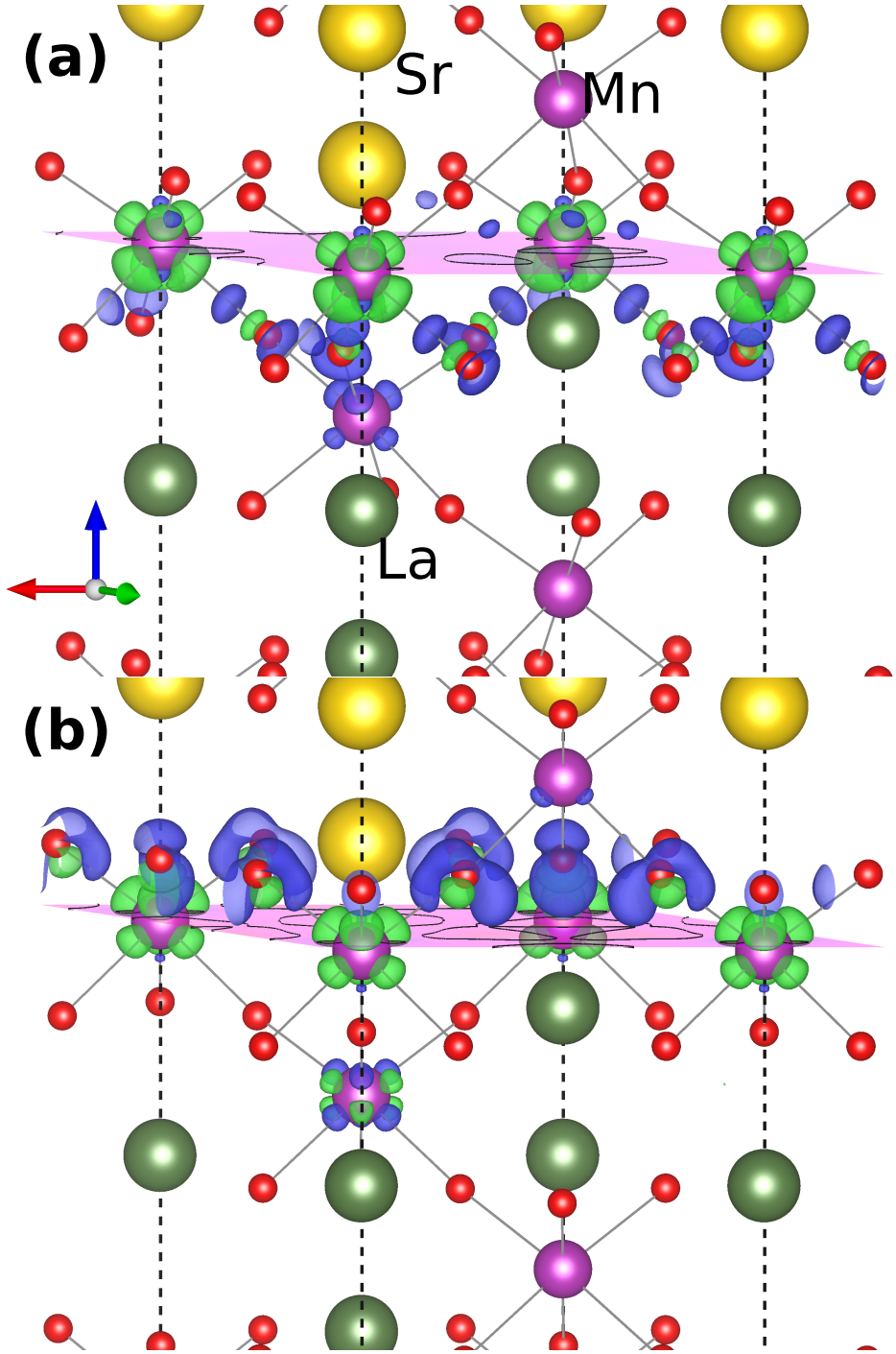

Supplementary Figure 5. Charge density difference at the interface in the superlattice (a) with octahedral tilts and (b) without octahedral tilts. Yellow and cyan colors represent charge accumulation and depletion, respectively. The isovalues are set to 0.01 electrons/Å^3.

[4] Keshavarz, S. *et al.* Exchange interactions of $CaMnO_3$ in the bulk and at the surface. *Phys. Rev. B* **95**, 115120 (2017).

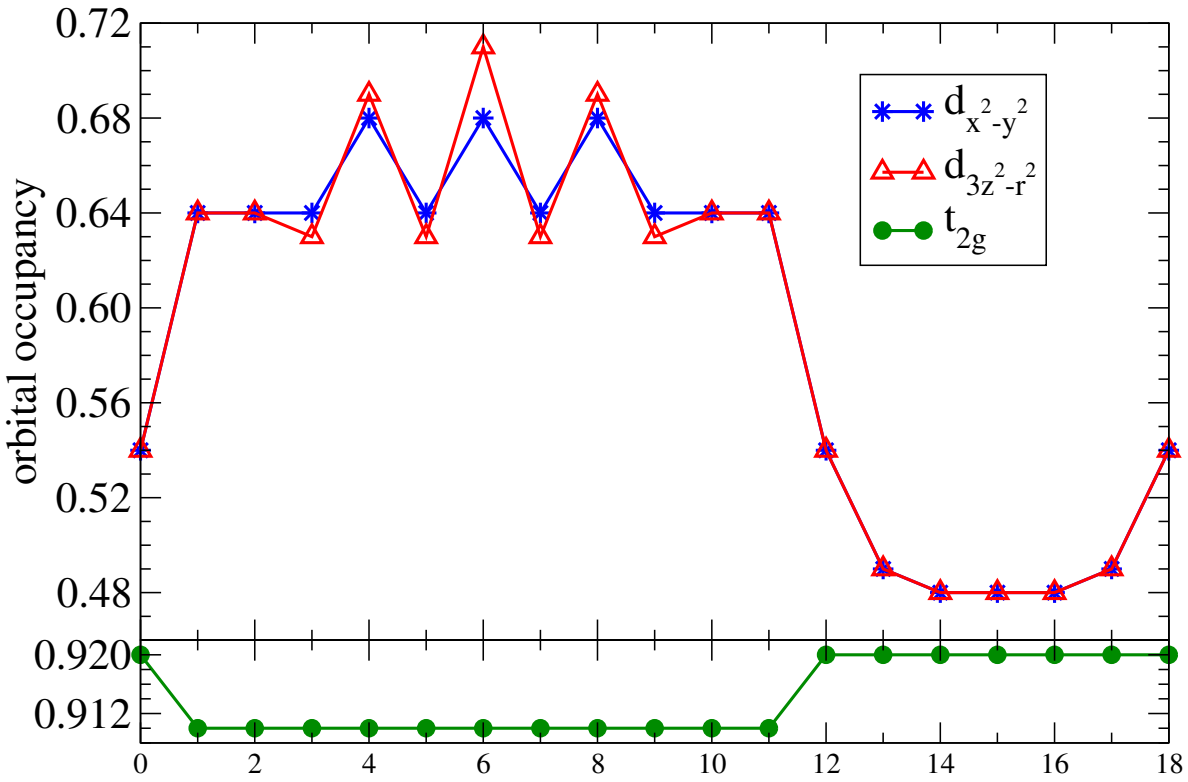

Supplementary Figure 6. Occupations of the Mn-3*d* states across the superlattice, projected over real spherical harmonics. Notice that the rigid step observed for the t_{2g} states reflects the precision of this calculation, i.e. 0.01.

[5] Glazer, A. M. The classification of tilted octahedra in perovskites. *Acta Crystallogr. Sect. B* **28**, 3384–3392 (1972).

[6] Takeda, T. & Ohara, S. Magnetic structure of the cubic perovskite type $SrMnO_3$. *J. Phys. Soc. Jpn* **37**, 275 (1974).

[7] Ricca, C., Timrov, I., Cococcioni, M., Marzari, N. & Aschauer, U. Self-consistent site-dependent dft+u study of stoichiometric and defective $srmno_3$. *Phys. Rev. B* **99**, 094102 (2019).

[8] Moussa, F. *et al.* Spin waves in the antiferromagnet perovskite $lamno_3$: A neutron-scattering study. *Phys. Rev. B* **54**, 15149–15155 (1996).

[9] Varignon, J., Bibes, M. & Zunger, A. Origin of band gaps in 3d perovskite oxides. *Nat. Commun.* **10**, 1658 (2019).

[10] Lee, J. H., Delaney, K. T., Bousquet, E., Spaldin, N. A. & Rabe, K. M. Strong coupling of Jahn-Teller distortion to oxygen-octahedron rotation and functional properties in epitaxially

strained orthorhombic lamno$_3$. *Phys. Rev. B* **88**, 174426 (2013).

[11] Mellan, T. A., Corà, F., Grau-Crespo, R. & Ismail-Beigi, S. Importance of anisotropic coulomb interaction in $LaMnO_3$. *Phys. Rev. B* **92**, 085151 (2015).

[12] Schmitt, M. M., Zhang, Y., Mercy, A. & Ghosez, P. Electron-lattice interplay in $LaMnO_3$ from canonical Jahn-Teller distortion notations. *Phys. Rev. B* **101**, 214304 (2020).

[13] Chen, H. & Millis, A. Charge transfer driven emergent phenomena in oxide heterostructures. *J. Phys.: Condens. Matter* **29**, 243001 (2017).

[14] Bhattacharya, A. *et al.* Metal-insulator transition and its relation to magnetic structure in $(LaMnO_3)_{2n}/(SrMnO_3)_n$ superlattices. *Phys. Rev. Lett.* **100**, 257203 (2008).

[15] Nanda, B. R. K. & Satpathy, S. Electronic and magnetic structure of the $(LaMnO_3)_{2n}/(SrMnO_3)_n$ superlattices. *Phys. Rev. B* **79**, 054428 (2009).

[16] Dong, S. & Dagotto, E. Quantum confinement induced magnetism in $LaNiO_3$-$LaMnO_3$ superlattices. *Phys. Rev. B* **87**, 195116 (2013).

[17] Nakao, H. *et al.* Charge disproportionation of Mn $3d$ and O $2p$ electronic states depending on strength of $p-d$ hybridization in $(LaMnO_3)_2/(SrMnO_3)_2$ superlattices. *Phys. Rev. B* **98**, 245146 (2018).

[18] Sun, J., Ruzsinszky, A. & Perdew, J. P. Strongly constrained and appropriately normed semilocal density functional. *Phys. Rev. Lett.* **115**, 036402 (2015).

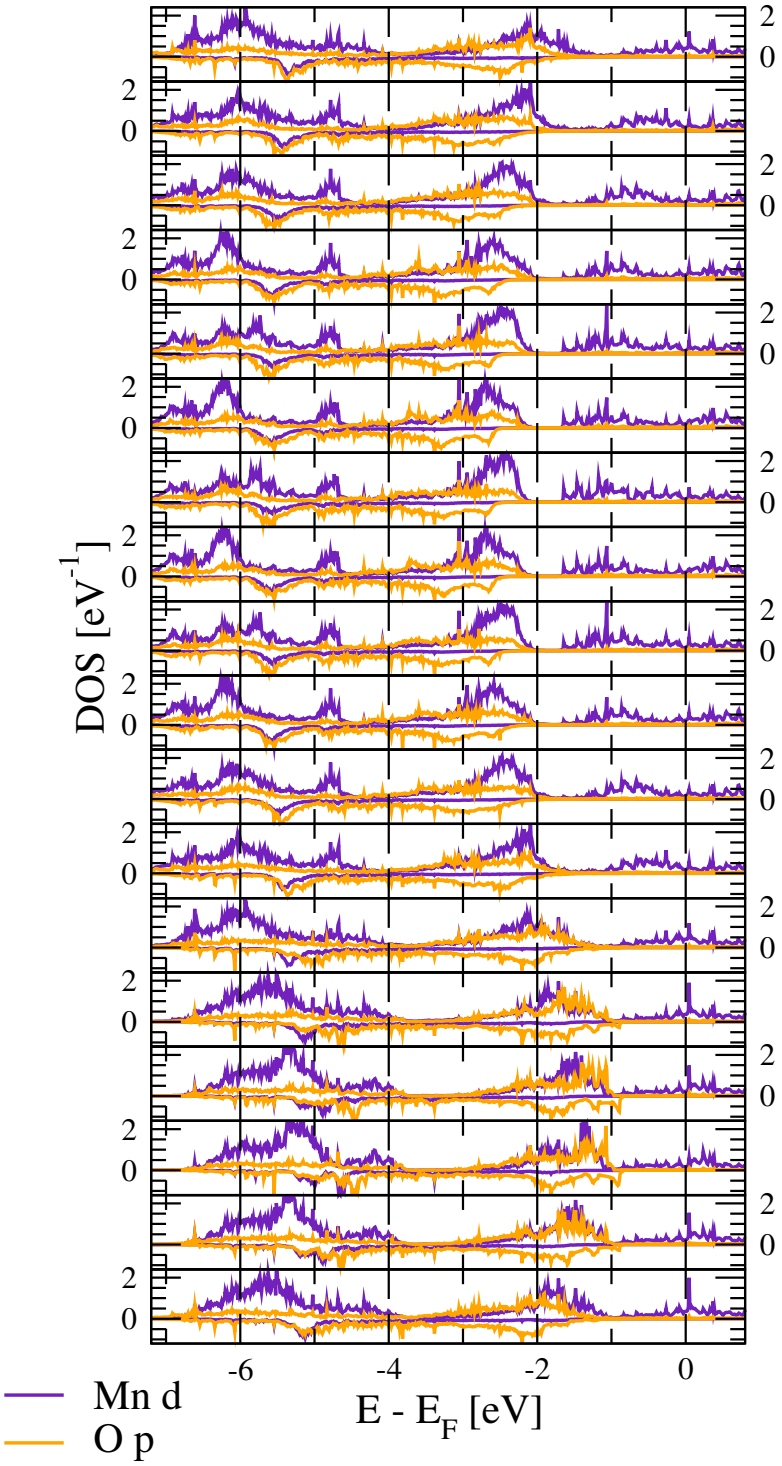

Supplementary Figure 7. Projected density of states for Mn-*d* and O-*p* electrons, resolved for each Mn-layer of the superlattice. Notice that the oxygens belong to intermediate layers between two Mn layers, but for visualization purposes we show them in the same plot used for Mn atom just below them. For example, in the topmost graph, alongside the Mn-*d* states of layer 0, we show the O-*p* states for atoms between layer 0 and layer 1.

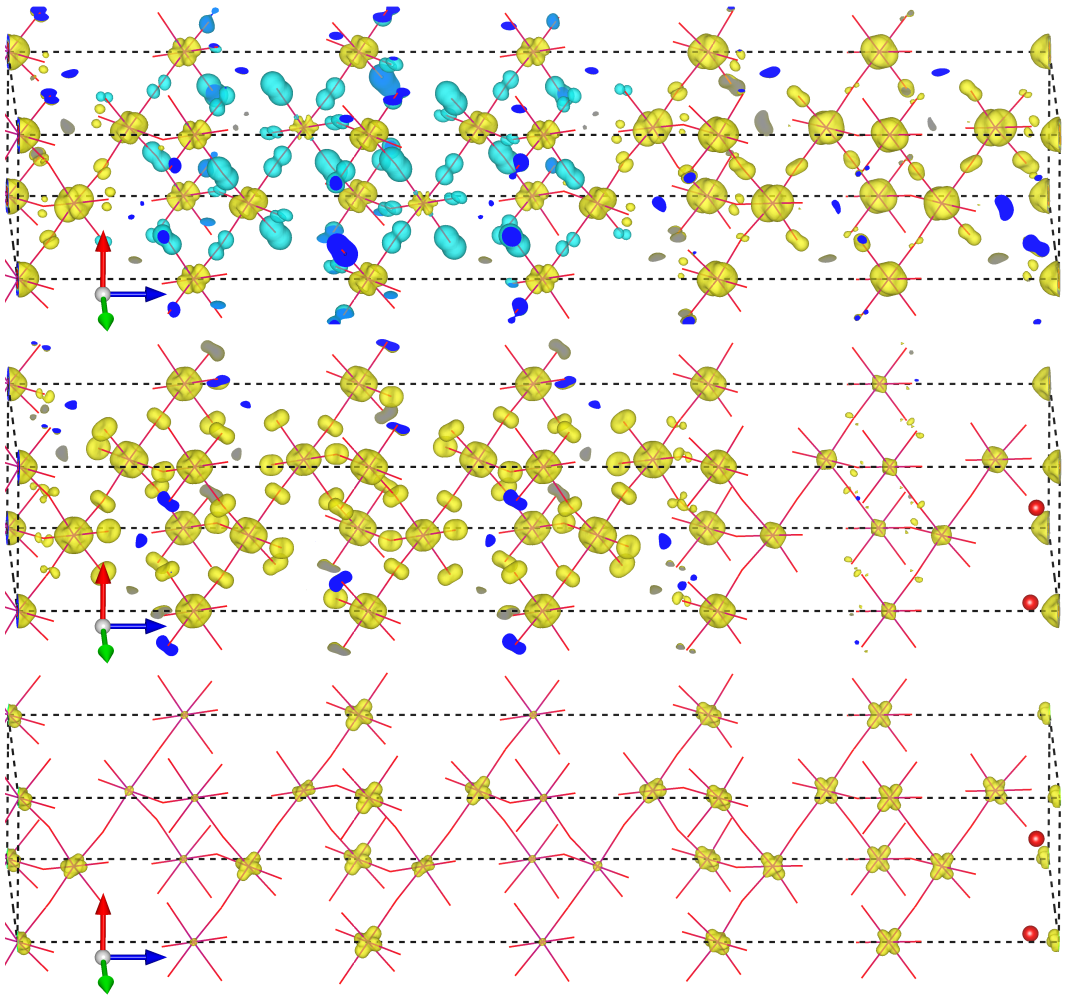

Supplementary Figure 8. Magnetization density distribution in direct-space for three different energy ranges, namely $(-5.95\ ;\ -5.35)$ eV, $(-2.52\ ;\ -2.00)$ eV, and $(-0.36\ ;\ 0.00)$ eV, shown in the top, middle and bottom panels respectively. The orbital character is roughly $d_{x^2-y^2}$ throughout the whole $LaMnO_3$ region; $d_{z^2-x^2}$ at the interface; $d_{3z^2-r^2}$ in the subsequent layer; $d_{y^2-z^2}$ in the remaining $SrMnO_3$ region.

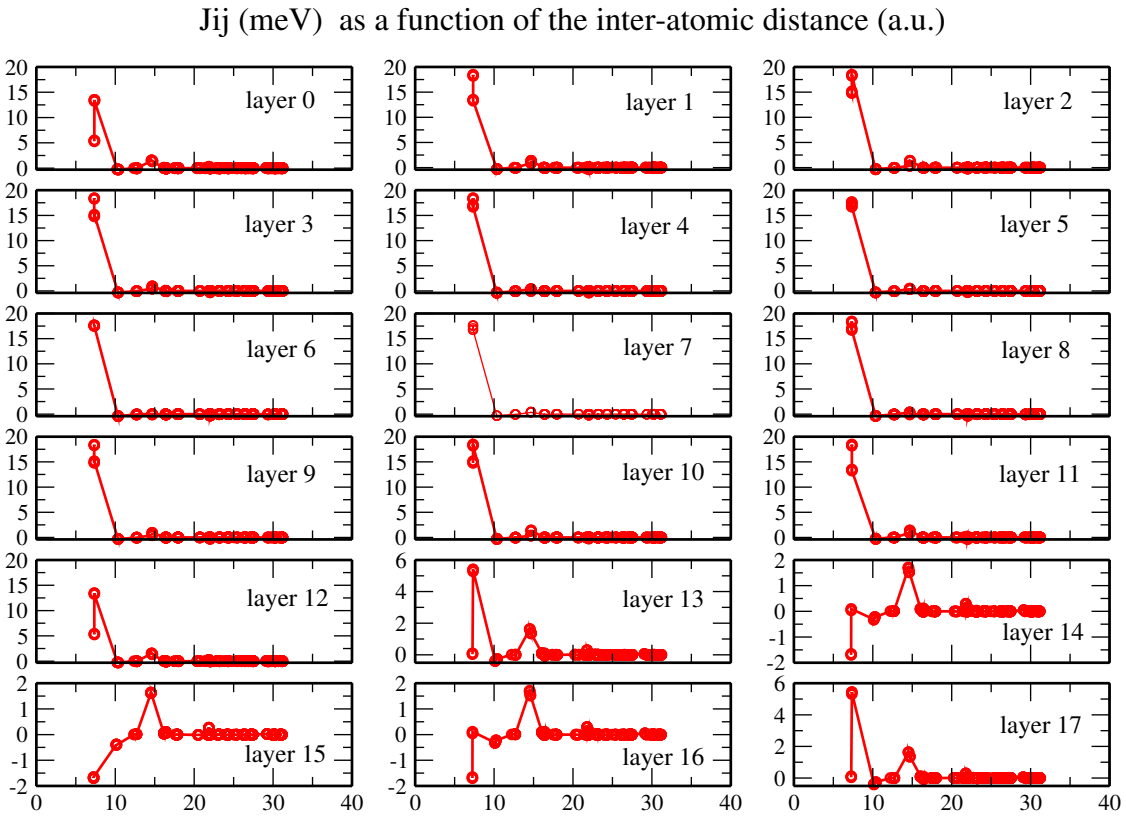

Supplementary Figure 9. Inter-atomic exchange parameters between Mn-3d states in different layers across the superlattice. The layers are numbered with respect to Fig. 1 of the main text, as elsewhere in the manuscript. Therefore, layers 0 and 12 are the interfacial layers, while layers 6 and 15 are the inner-most layers in the $LaMnO_3$ and $SrMnO_3$ regions, respectively.

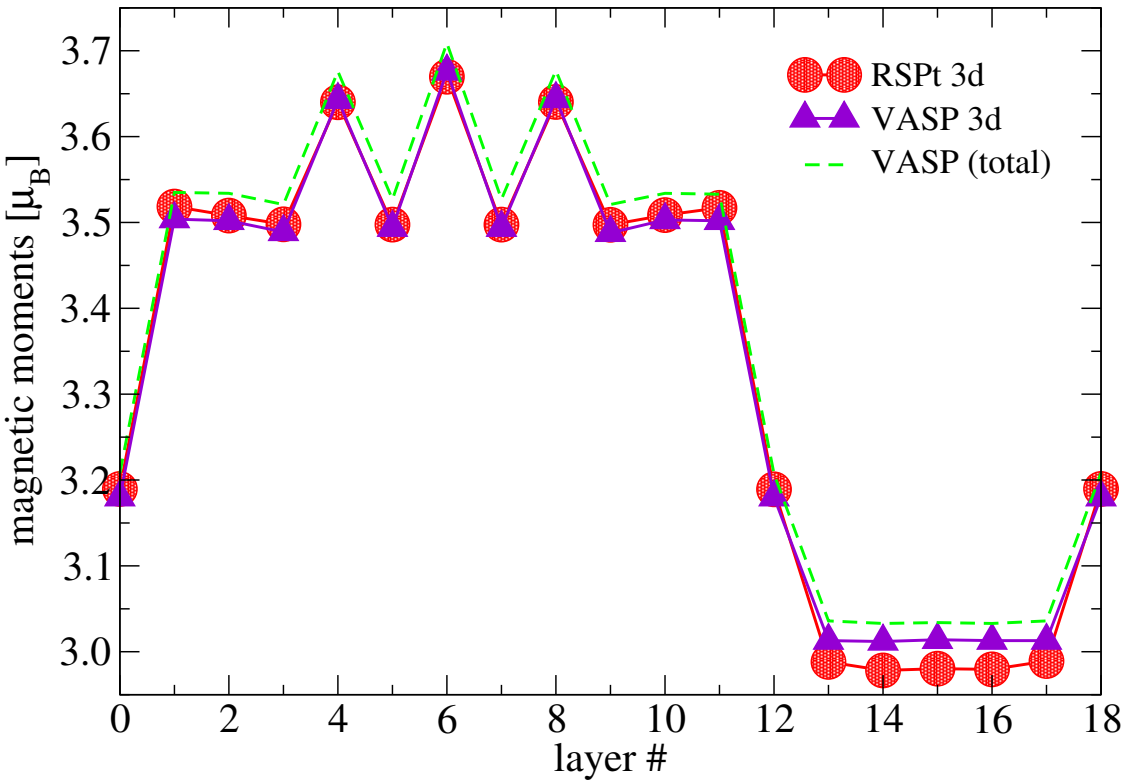

Supplementary Figure 10. Layer-resolved magnetic moments at the Mn sites as computed by VASP and RSPt.

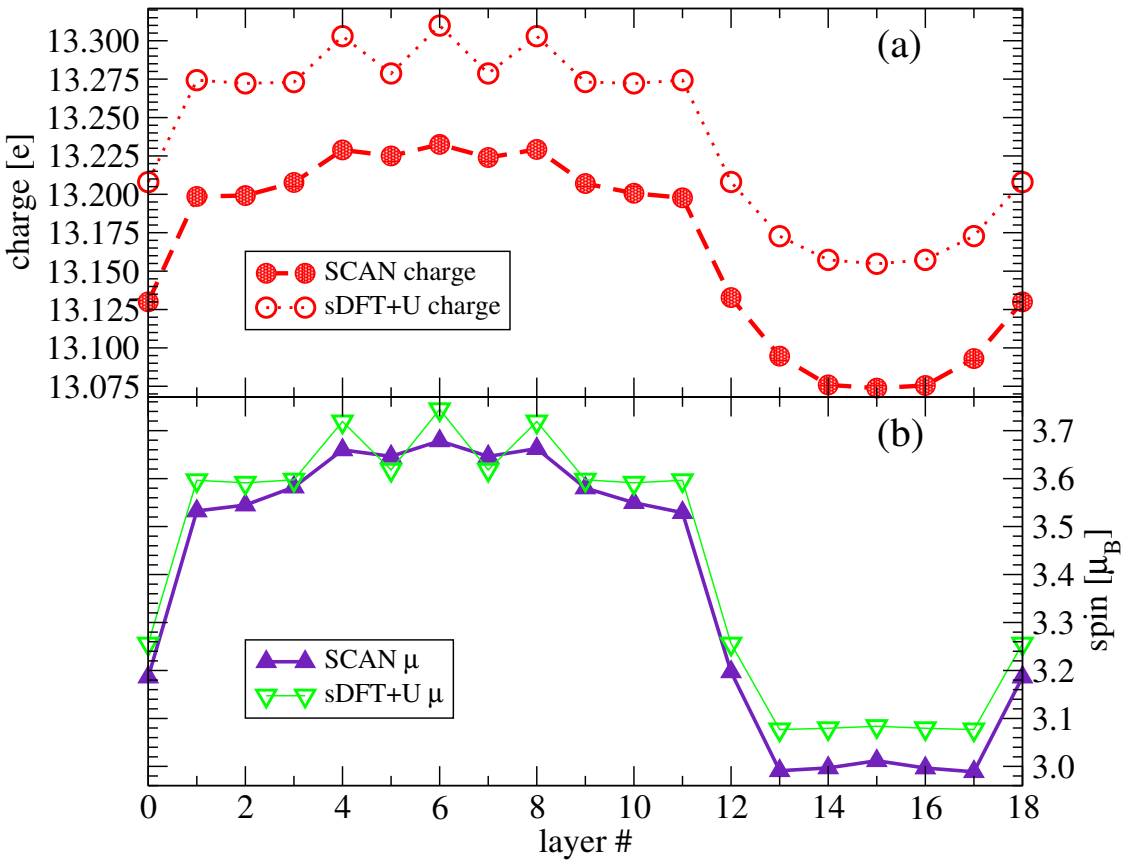

Supplementary Figure 11. Layer-resolved magnetic moments at the Mn sites as computed with the SCAN functional on the $R\bar{3}c$ cell (with the $a^-a^-a^-$ tilting pattern).